SF2A 2025
A. Siebert, K. Baillié, M. Béthermin, F. Cantalloube, E. Josselin, N. Lagarde, J. Malzac, J. Richard, L. Selliez, O. Venot (eds)

DETECTING NON-KERR SIGNATURE IN SGR A* FLARES WITH CURRENT AND FUTURE INSTRUMENTS

N. Aimar[1], J. a. L. Rosa[2] and H. L. Tamm[2]

Abstract. The heart of our galaxy harbors a supermassive compact object named Sagittarius A* (Sgr A*), with a mass of 4.3 million solar masses which regularly produces radiation bursts known as flares, occurring around 10 gravitational radii, which situates them within the strong gravitational regime. Despite significant astrophysical uncertainties, these flares provide a unique opportunity to investigate space-time properties, particularly by employing polarization measurements. This is because polarization is influenced by the curvature of space-time and therefore can be utilized to unveil the properties of the compact object. We studied three families of non-rotating exotic compact object (ECO) that are black hole mimickers: 1) boson stars, 2) gravastars and 3) fluid sphere. All the configurations studied present additional images compared to Schwarzschild (plunge-through images or multiple light rings) which affects both the observed polarization fraction and Electric Vector Position Angle (EVPA) compared to the black hole solution.

We investigated the detectability of these signatures by fitting synthetic flare data with a hot spot model and the previously mentioned metrics, using statistical criteria. We found that with the current uncertainties of the GRAVITY instrument we can asses if the background metric is Schwarzschild or an ECO but we can not recover the correct metric. However, with the future upgrade of the instrument GRAVITY+ and its better sensitivity, the detectability increase significantly.

However, astrophysical uncertainties can mimic such signature, meaning that we need a better understanding of the flares' astrophysics before claiming a detection of an ECO signature from Sgr A* flares.

Keywords: Black hole physics, Relativistic processes, Polarization, Accretion disk, Radiative transfer

1 Introduction

The center of our galaxy hosts Sagittarius A* (Sgr A*), a supermassive compact object of $(4.297 \pm 0.012) \times 10^6$ solar masses at a distance of only $8,277 \pm 9$ pc (GRAVITY Collaboration et al. 2022). It is surrounded by the so-called S-Star cluster, in which stars orbit around the compact object and allowed to test General Relativity (GR). However, the closest star detected so far is still at a few thousand gravitational radii r_g, i.e. not in the strongest gravitational regime. The current observational state-of-the-art cannot fully constrain the nature of the supermassive compact object at the center of the galaxy (De Laurentis et al. 2023).

The Event Horizon Telescope (EHT) has provided the first horizon-scale image of Sgr A*, the (Event Horizon Telescope Collaboration et al. 2022a). This landmark observation opens the door to testing the nature of compact objects in the strong gravity regime. While the image is broadly consistent with the predictions of GR for a Kerr black hole, it does not definitively rule out the existence of exotic compact objects (ECOs) that mimic many black hole features but lack an event horizon (Event Horizon Telescope Collaboration et al. 2022b; Carballo-Rubio et al. 2022; Vagnozzi et al. 2023; Shaikh 2023).

Since 2001, outbursts of radiation called flares have been detected from Sgr A*. The GRAVITY Collaboration reported the detection of orbital motion for Sgr A* flares (GRAVITY Collaboration et al. 2018) at only a few r_g, in the strong-field regime. They are thus an ideal object to study and constrain the nature of Sgr A*. Although the effects of spin or ECOs metrics on the flare light curves and astrometry are too small to be detected. The detection of polarization of Sgr A* flares in NIR (Gravity Collaboration et al. 2023) brought new observational constraints. We thus here investigated the imprints of ECOs on Sgr A* flares' polarization and their detectability using the ray-tracing code `GYOTO` (Aimar et al. 2024).

[1] CENTRA, Faculdade de Engenharia, Universidade do Porto, s/n, R. Dr. Roberto Frias, 4200-465 Porto, Portugal
[2] Institute of Physics, University of Tartu, W. Ostwaldi 1, 50411 Tartu, Estonia

2 Non-rotating Exotic Compact Objects

We studied 3 families of ECOs: boson stars, fluid spheres and gravastars.

2.1 Solitonic Boson Star

Scalar Boson stars consist of localized solutions of self-gravitating scalar fields. They are found as solutions of the Einstein-Klein-Gordon theory with a complex scalar field ϕ, and a scalar potential V. Different Boson star models are obtained depending on the form of the potential V. In particular, solitonic Boson stars are described by a potential of the form $V = \mu^2|\phi|^2\left(1 - |\phi|^2/\alpha^2\right)^2$, where μ is a constant that plays the role of the mass of ϕ and α is a constant free parameter of the model (see Rosa et al. 2023, 2025, for more details).

We consider three numerical solutions of solitonic Boson stars with different compactness, a dilute model (BS1), a model close to the ultra-compact regime (BS2), and an ultra-compact model (BS3) described in detail in Rosa et al. (2023).

2.2 Fluid Sphere

Relativistic Fluid spheres are solutions to Einstein's field equations in the presence of an isotropic perfect fluid. Restricting our analysis to smooth solutions where the star's surface R is the radius for matching interior and exterior solutions with constant energy density, we find bound-photon orbits form when $R \leq 3M$. At $R = 3M$, there is a single degenerate bound-photon orbit, and a singularity occurs if $R \leq 2.25M$. More details about this model can be found in Ref. Tamm & Rosa (2024). Three models were studied in Tamm & Rosa (2024) with $R = 2.25M$ (FS1), $R = 2.5M$ (FS2), and $R = 3M$ (FS3).

2.3 Gravastar

Similarly to relativistic Fluid spheres, Gravastars, are solutions of the Einstein's field equations in the presence of an isotropic perfect fluid. In the case of Gravastars, this fluid is exotic, satisfying an equation of state of the form $p = -\rho$, where p is the isotropic pressure and ρ is the energy density. These solutions develop a pair of bound-photon orbits whenever the radius R of the surface of the Gravastar satisfies the condition $R \leq 3M$, with the limiting case $R = 3M$ corresponding to a single degenerate bound-photon orbit. More details about this model can be found in Ref. (Rosa et al. 2024). We fixed $\alpha = 1$ for numerical reason and selected three configurations: a model with $R = 3M$ (GS1), $R = 2.5M$ (GS2) and $R = 2.01M$ (GS3).

3 Flares polarization in ECO space-time

3.1 Contribution of additional images in ECOs metrics

The key difference between the Schwarzschild background and the ECOs studied is the presence of additional images as seen in the left panel of Fig. 1 which shows the time integrated images for Stokes I (first column), Stokes Q (second column) and Stokes U (third column) for the three boson star configuration at 20°inclination. These additional images can be from a second light ring or from geodesics which penetrate the interior of the compact objects and are called plunge-through images. Note that the model BS1 only shows the primary image.

Figure 1's left panel illustrates that the polarization of these additional images closely resembles the polarization of secondary images in the Schwarzschild scenario. Although their impact on total intensity (Stokes I) is always positive, their influence on total polarized flux (Stokes Q and U) can vary in sign. Consequently, they modify both the Electric Vector Position Angle (EVPA) as defined by Stokes Q and U, and the linear polarization fraction $lp = \frac{\sqrt{Q^2+U^2}}{I}$. Additionally, these images' contributions change over the orbital period, which accounts for the smaller second loop in the normalized QU-plane for the BS2 and BS3 models compared to Schwarzschild (see the right panel of Fig. 1).

3.2 Detectability of ECOs

3.2.1 Methodology

To assess metric detectability, we fit simulated data using all metrics and compare results via the *Bayesian Information Criterion* (BIC). The optimal fit yields the lowest χ^2_{red}, while the second-best fit has the next

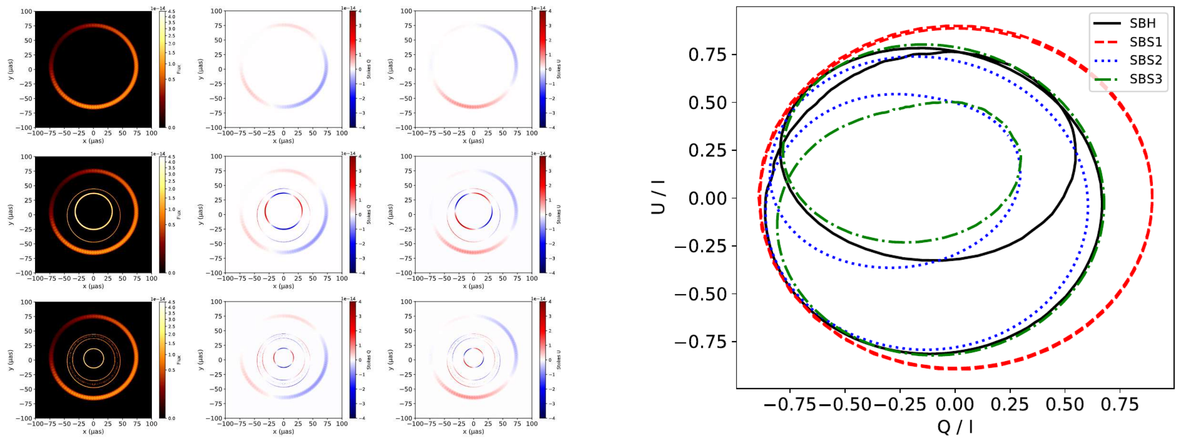

Fig. 1. Left: Time integrated images of a hot spot orbiting the BS1 model (**top**), BS2 model (**middle**) and BS3 model (**bottom**) for Stokes I (first column), Stokes Q (second column) and Stokes U (third column) at an inclination of 20°. **Right:** Evolution of the Stokes parameters on the normalized QU-plane during the orbital period for a Schwarzschild BH and models BS1-BS3 for an inclination of 20°.

lowest. To compare these and evaluate detectability, we calculate the BIC-based Bayes factor K (Wagenmakers 2007).

$$\log_{10} K = \log_{10}\left[\exp\left(\frac{\Delta BIC}{2}\right)\right]. \tag{3.1}$$

As the impact of the plunge-through images (induced by the background metrics) may not be large enough to result in a significant better fit, in terms of $\chi^2_{\rm red}$, for one metric compared to the others, we thus define three detectability outcomes according to the value of $\log_{10} K$ and following the Kass & and (1995) scale: $\log_{10} K < 1$ **not detectable** symbolized by a red cross; $1 \leq \log_{10} K \leq 2$ **partially detectable** symbolized by an orange tilde; $\log_{10} K > 2$ **detectable** symbolized by a green check-mark.

3.2.2 Results

We initially assessed how detectable the studied ECO metrics are given current GRAVITY uncertainties. We applied the previously explained method to each generated dataset, with the outcomes displayed in Fig. 2. This table shows for each simulated data in a given background metric (each line), the best-fitted metric (second column), the associated $\chi^2_{\rm red}$ and BIC in the next two columns. Columns five and six show the second best-fitted metric and the BIC-based Bayes factor $\log_{10} K$ between the latter and the best-fitted metric, respectively. Finally, the last two columns highlight the detectability of the metric used to generate the simulated data compared to all other metrics and compared to Schwarzschild according to the BIC-based Bayes factor values respectively.

Background metric of data	best fitted metric	$\chi^2_{\rm red}$	BIC	2nd best fitted metric	$\log_{10} K$	detectable	exclude Sch
Schwarzschild	Schwarzschild ✓	0.94	60	Gravastar 1	1.1	~	
Boson star 2	Boson star 2 ✓	1.03	65	Fluid sphere 3	2.5	✓	✓
Boson star 3	Fluid sphere 2 ✗	0.71	50	Boson star 3	0.51	✗	✓
Fluid sphere 2	Fluid sphere 2 ✓	0.91	59	Boson star 3	0.56	✗	~
Fluid sphere 3	Fluid sphere 3 ✓	0.91	59	Boson star 3	0.28	✗	✓
Gravastar 1	Boson star 3 ✗	0.93	60	Gravastar 2	0.15	✗	✓
Gravastar 2	Gravastar 2 ✓	1.10	68	Gravastar 1	0.17	✗	✓
Gravastar 3	Schwarzschild ✗	1.00	64	Boson star 3	0.27	✗	✗

Fig. 2. Fit summary results for the studied metrics and Bayesian criteria with current GRAVITY uncertainties.

The main conclusion from Fig. 2 is that most of the metric signature can not be clearly detected with GRAVITY uncertainties. This is because the imprint of the various ECO's model are very similar to each other making it hard to detect. However, for most of them the fit of a hot spot in an ECO background are sufficiently better with any ECOs' model compared to Schwarzschild, so the latter can be excluded. This means that the impact of the plunge-through images into the polarization measurement is sufficiently important to exclude the Schwarzschild metric (if the data are in an ECO background) but not large enough (compared to the uncertainties) to distinguish one ECO metric from the other.

In 2026, the upgrade of the GRAVITY instrument called GRAVITY+ should enter in service. The expected improvement is a factor of ~ 7 in the S/N with respect to flux uncertainties (Bourdarot & Eisenhauer 2024). We therefore investigated how this improvement affects the detectability of the studied ECO models. We performed the same analysis as before with a seven times smaller uncertainty of the flux. Given the high level of photometric precision achieved, the influence of the plunge-through images, as induced by the various ECO models, exceeds the associated uncertainty. This leads to a considerably improved fit of the data when evaluated using the metric employed to generate the simulated data, as opposed to alternative metrics.

However, the model used in this study is very simplistic, with very little astrophysics, where most of the photometric properties are governed by relativistic effects like beaming, Doppler Boosting, and light bending. In reality, flares are much more complex with a lot of astrophysical uncertainties that mitigate detectability and can lead to an incorrect best-fit metric.

4 Conclusion

The key difference between the ECOs studied here and ordinary black holes is the presence of plunge-through images. These images share polarization characteristics with the secondary image in Schwarzschild space-time, affecting both the observed EVPA and the polarization fraction.

We assessed the detectability of a given metric by generating simulated data for it and performing 8 fits (one per metric analyzed). The metric with the least $\chi^2_{\rm red}$ is deemed the best fit. Detectability is determined by comparing the BIC-based Bayes factor K between the best and other metrics; if the minimum $\log_{10} K$ difference exceeds 2, the metric is considered detectable.

Plunge-through images' polarization imprints are comparable to the GRAVITY instrument's current measurement uncertainties. As such, only the Boson star 2 model can be clearly distinguished (see Fig. 2). Despite these uncertainties, Schwarzschild fits to simulated data in an ECO metric perform poorly, allowing us to reject the Schwarzschild metric. We also anticipate the detection ability of ECOs with the GRAVITY+ upgrade. With flux uncertainties about 7 times smaller, all metrics should be clearly identifiable. However, the hot spot model has limited astrophysics that might still imitate the space-time signatures.

Thank you to the organizers of the SF2A 2025!

References

Aimar, N., Paumard, T., Vincent, F. H., Gourgoulhon, E., & Perrin, G. 2024, Classical and Quantum Gravity, 41, 095010

Bourdarot, G. & Eisenhauer, F. 2024, arXiv e-prints, arXiv:2410.22063

Carballo-Rubio, R., Di Filippo, F., Liberati, S., & Visser, M. 2022, J. Cosmology Astropart. Phys., 2022, 055

De Laurentis, M., de Martino, I., & Della Monica, R. 2023, Reports on Progress in Physics, 86, 104901

Event Horizon Telescope Collaboration, Akiyama, K., Alberdi, A., et al. 2022a, ApJ, 930, L12

Event Horizon Telescope Collaboration, Akiyama, K., Alberdi, A., et al. 2022b, ApJ, 930, L17

Gravity Collaboration, Abuter, R., Aimar, N., et al. 2023, A&A, 677, L10

GRAVITY Collaboration, Abuter, R., Aimar, N., et al. 2022, A&A, 657, L12

GRAVITY Collaboration, Abuter, R., Amorim, A., et al. 2018, A&A, 618, L10

Kass, R. E. & and, A. E. R. 1995, Journal of the American Statistical Association, 90, 773

Rosa, J. a. L., Aimar, N., & Liis Tamm, H. 2025, arXiv e-prints, arXiv:2504.02472

Rosa, J. a. L., Cordeiro, D. S. J., Macedo, C. F. B., & Lobo, F. S. N. 2024, Phys. Rev. D, 109, 084002

Rosa, J. a. L., Macedo, C. F. B., & Rubiera-Garcia, D. 2023, Phys. Rev. D, 108, 044021

Shaikh, R. 2023, MNRAS, 523, 375

Tamm, H. L. & Rosa, J. a. L. 2024, Phys. Rev. D, 109, 044062

Vagnozzi, S., Roy, R., Tsai, Y.-D., et al. 2023, Classical and Quantum Gravity, 40, 165007

Wagenmakers, E.-J. 2007, Psychonomic Bulletin & Review, 14, 779